Journal of Volcanology and Geothermal Research 178 (2008) 708–718

Contents lists available at ScienceDirect

Journal of Volcanology and Geothermal Research

journal homepage: www.elsevier.com/locate/jvolgeores

Buried rhyolites within the active, high-temperature Salton Sea geothermal system

Axel K. Schmitt [a,*], Jeffrey B. Hulen [b]

[a] Department of Earth and Space Sciences, UCLA, Los Angeles, CA 90095-1567, USA
[b] Consulting Geologist, 1375 Talachiro Circle, Ivins, UT 84738, USA

ARTICLE INFO

Article history:
Received 6 May 2008
Accepted 1 September 2008
Available online 9 September 2008

Keywords:
rifting
volcanism
zircon
Gulf of California
Pleistocene

ABSTRACT

Previously unrecognized pulses of rhyolite volcanism occurred in the Salton Trough between 420±8 ka and 479±38 ka (2σ), based on high-spatial resolution U–Pb zircon geochronology. Presently, these rhyolite lavas, tuffs and shallow subvolcanic sills are buried to depths between ~1.6 and 2.7 km at ambient temperatures between 200 and 300 °C, and are overprinted by propylitic to potassic hydrothermal alteration mineral assemblages consisting of finely intergrown quartz, K-feldspar, chlorite, epidote, and minor pyrite. Alteration resistant geochemical indicators (whole-rock Nd-isotopes, zircon oxygen-isotopes) reveal that these rhyolites are derived from remelting of MORB-type crust that was chilled and hydrothermally altered by deep-circulating hydrothermal waters. U–Pb zircon dating confirms the presence of Bishop Tuff in well State 2-14 at ~1.7 km depth, approximately 5 km NE of the geothermal wells that penetrated the buried rhyolites. These results indicate accelerated subsidence towards the center of the Salton Trough, increasing from 2.2 mm/a to 3.8 mm/a. Based on these results, the present-day Salton Sea geothermal field is identified as a focus zone of episodic rhyolitic volcanism, intense heat flow and metamorphism that predates present-day geothermal activity and Holocene volcanism by at least ~400 ka.

1. Introduction

The Salton Trough is the onshore extension of the Gulf of California, a zone of transtensional to rift basin formation and embryonic sea-floor spreading that has developed since the Pliocene (Lonsdale, 1989; Dorsey et al., 2007). The region hosts geothermal systems that cumulatively produce nearly 1 TWh/yr of electricity (Bertani, 2005) in a series of geothermal fields (GFs) and known resources that comprise the Salton Sea (SSGF), Brawley, Heber, East Mesa, and Cerro Prieto. Despite conspicuously elevated regional heat flow within the basin, surficial evidence of magmatism is sparse and restricted to small rhyolite domes, the Salton Buttes, along the southern shore of the Salton Sea, and the composite dacite dome of Cerro Prieto (Fig. 1). Xenoliths in Salton Buttes lavas, and dikes and sills in SSGF geothermal wells provide evidence for bimodal magmatism and granitic intrusions at depth (Robinson et al., 1976; Schmitt and Vazquez, 2006).

A heretofore poorly understood manifestation of rift-related volcanism in the Salton Trough are subsurface rhyolites that are present as ~100–300 m thick intersections in three SSGF wells at depths between ~1.6 and 2.7 km (Fig. 2; Hulen et al., 2003). Hulen and Pulka (2001) and Hulen et al. (2002, 2003) discovered these buried rhyolite lavas and pyroclastic rocks, and stressed their importance for the magmatic evolution of the SSGF. In addition, a distal deposit of Bishop Tuff (770.4±3.6 ka; Sarna-Wojcicki et al., 2000 recalculated by Crowley et al., 2007) was described for SSGF research well State 2-14 at 1.7 km depth (Herzig and Elders, 1988) and represents an important temporal marker horizon within the Salton Trough rift basin sequence (Izett et al., 1970). Reliable age constraints for these rhyolites are essential for quantifying sedimentation, subsidence and thermal evolution of the SSGF, but have so far been unavailable. High ambient temperatures (~200–390 °C), and pervasive fluid flow in the SSGF frequently causes moderate to strong alteration of primary minerals and renders futile most conventional dating methods.

Here, we present U–Pb zircon ages which record magmatic crystallization for SSGF subsurface rhyolites. Our results reveal previously unknown rhyolitic volcanism in the Salton Trough in the Pleistocene, significantly older than previously known from ages of surface volcanic rocks, and confirm the presence of Bishop Tuff in the SSGF that was previously postulated based on chemical correlations. These results allow a re-evaluation of sedimentation and subsidence rates and indicate approximately twofold accelerated vertical displacement towards the center of the Salton Trough, over a few km lateral distances. This requires substantial vertical offsets by high-angle normal faulting. Fluid-inert geochemical tracers (whole-rock Nd-isotopes, zircon oxygen-isotopes) underline the compositional and genetic kinship between subsurface and surface rhyolites in the SSGF. Based on these tracers, we develop a petrogenetic model that involves localized injection of basaltic magma that episodically triggered pulses of rhyolite volcanism by remelting of juvenile basaltic crust, and deep-reaching hydrothermal activity over at least 400 ka, orders

* Corresponding author. Tel.: +1 310 206 5760.
E-mail address: axel@oro.ess.ucla.edu (A.K. Schmitt).

0377-0273/$ – see front matter © 2008 Elsevier B.V. All rights reserved.
doi:10.1016/j.jvolgeores.2008.09.001

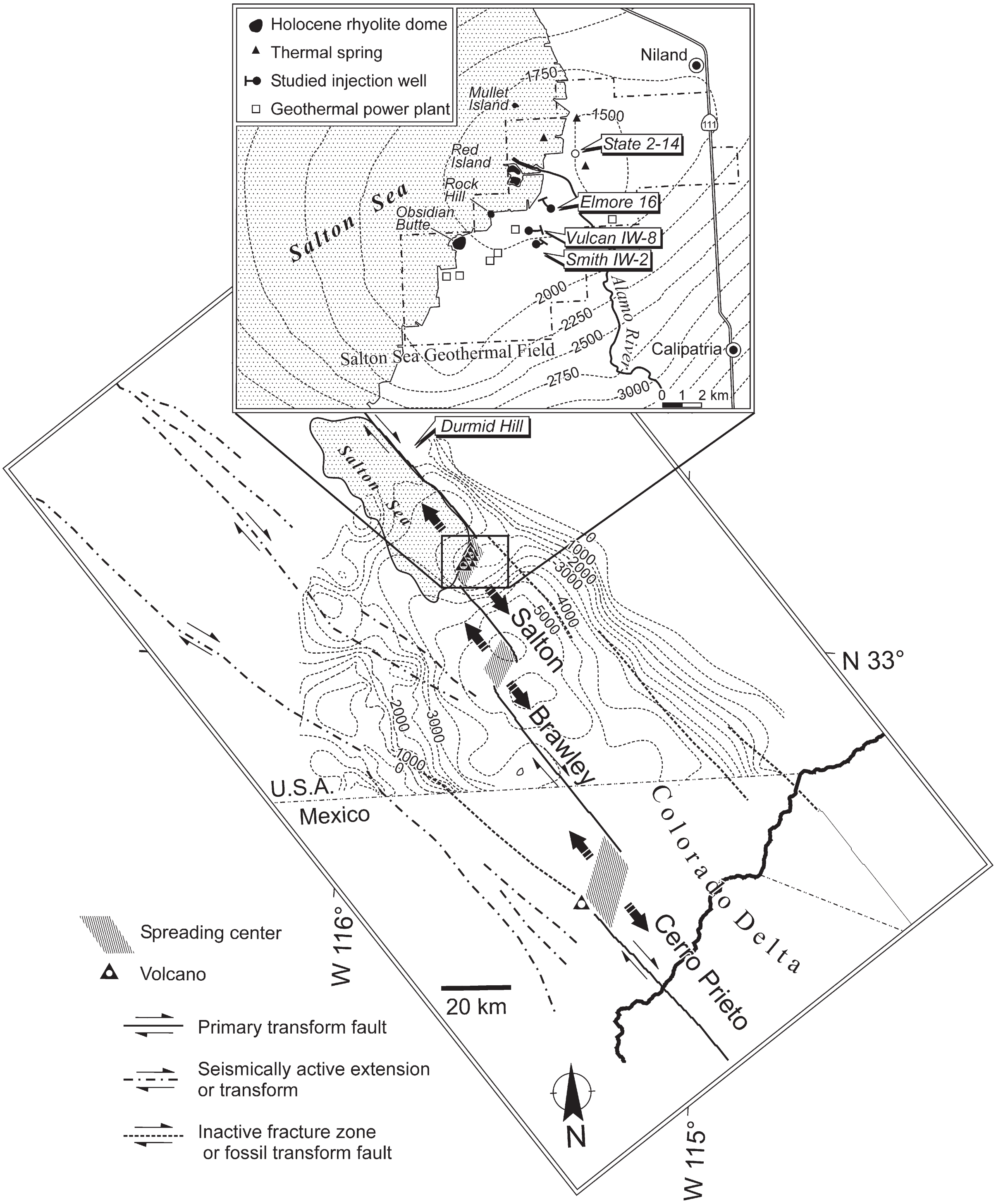

Fig. 1. Geologic and tectonic sketch map showing major strike slip faults and pull-apart basins in the Salton Trough and Mexicali Valley (after Lonsdale, 1989). Isolines show depths in m to rocks with seismic velocities >5.6 km/s that underlie unmetamorphosed sediments (Fuis and Kohler, 1984, after Severson, 1987).

of magnitude older than estimates for the age of the present-day shallow SSGF hydrothermal system (Kasameyer et al., 1984; Zukin et al., 1987; Heizler and Harrison, 1991).

2. Geologic background

The ~30 km-wide and ~100-km long Salton Trough is a NW–SE trending topographic depression generated by oblique extension and subsidence within a pull-apart basin that developed between strands of the San Andreas fault system (Fig. 1; Elders et al., 1972; Lonsdale, 1989). Sedimentation occurred in rapidly subsiding narrow continental rift basins, and transient marine seaways developed during late Miocene to Pliocene, culminating in deposition of voluminous deltaic deposits of the Colorado River since ~5 Ma (Dorsey et al., 2007). The margins of the present-day depocenter in the Salton Trough are affected by recent faulting and uplift along the San Andreas–Imperial fault system, causing erosion and reworking of older sediments (Dorsey et al., 2007). Throughout the Pleistocene and Holocene,

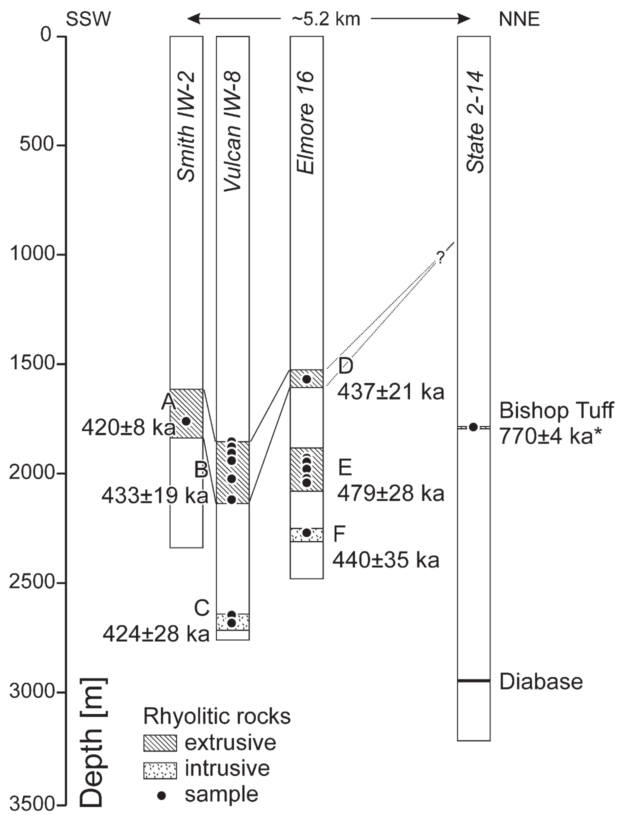

Fig. 2. Schematic well logs showing presence of volcanic rocks in studied Salton Sea Geothermal Field wells (after Hulen and Pulka, 2001; Hulen, unpublished data; Herzig and Elders, 1988). All ages are U–Pb zircon-model ages, except for (*) which is the $^{40}Ar/^{39}Ar$ sanidine age for Bishop Tuff (Sarna-Wojcicki et al., 2000, recalculated by Crowley et al., 2007). Letters refer to panels in Fig. 4. All age uncertainties quoted at 2σ level.

damming by the Colorado River delta isolated the Salton Trough from marine incursions, but the river episodically drained into the Trough, creating ephemeral lakes. Pre-historic Lake Cahuilla, with its well preserved shorelines, is the latest natural expression of lake formation. Based on ^{14}C-dating of tufa, Lake Cahuilla existed at least between ~20,500 a BP and 1300 a BP (Li et al., 2008), and had evaporated prior to the accidental Colorado spill-over between 1905 and 1907 that created the Salton Sea (Sykes, 1937).

The thickness of clastic sedimentary basin fill of the Salton Trough increases sharply to >5 km in its axial zone (Fig. 1). This zone of maximal subsidence coincides with the Brawley seismic zone, widely thought to represent an oblique spreading center. (Fig. 1; Elders et al., 1972; Fuis et al., 1984). Seismic models suggest that low-density sediments are underlain by basement rocks and metamorphosed sediments, with seismic velocities >5 km/s. In the SSGF and vicinity, hydrothermal alteration and thermal metamorphism densified sediments (e.g., McDowell, 1987; McKibben and Hardie, 1997) so that they closely mimic basement in the depth ranges encompassed by the buried rhyolites and the Bishop Tuff that are the subject of our investigation (Fig. 1; Fuis and Kohler, 1984).

The present study focuses on six intersections of altered rhyolite that were penetrated deep in three geothermal wells drilled within the NE portion of the SSGF (Fig. 2). From SW to NE, these wells are: Smith IW-2 (extrusive rhyolite between 1600 and 1770 m depth), Vulcan IW-8 (extrusive rhyolite between 1860 and 2130 m; intrusive rhyolite between 2640 and 2670 m), and Elmore 16 (extrusive rhyolite between 1520–1580 m and 1850–2050 m; intrusive rhyolite between 2160 and 2280 m). Rock chips were sampled as mm-sized cuttings at ~3 m depth intervals during drilling, and made available for study by CalEnergy Operating Co. (see Figs. 1 and 2 for well locations and vertical extents of the volcanic sections within the wells). Interbedded with the rhyolites are sandstones, siltstones, mudstones and possibly marls deposited in fluvatile–lacustrine environments (Hulen and Pulka, 2001; Hulen et al., 2003). Fine-grained sedimentary rocks dominating the upper ~400 m sections of the wells provide an impermeable cap-rock for the underlying high-temperature hydrothermal system (Hulen and Pulka, 2001; Hulen et al., 2003). Beneath the cap, sediments comprise very fine-grained sandstone, siltstone and mudstone in subequal ratios that have been hydrothermally altered at still-prevailing temperatures ranging from 200–390 °C at depths >1 km (Hulen and Pulka, 2001; Hulen et al., 2003).

Based on microscopic inspection, two main varieties of massive altered rhyolite were identified: (1) extremely fine-grained (<5 µm), microcrystalline and largely aphyric rhyolite, that frequently preserves flow-banding and spherulitic devitrification textures, and (2) trachytoid, microcrystalline, sparsely phyric (5–10 µm crystal size) rhyolite. Both types of rhyolites show moderate to strong propylitic to potassic hydrothermal alteration, consisting dominantly of finely intergrown quartz, K-feldspar, chlorite, epidote and minor pyrite. Flow-banding and spherulitic devitrification textures are partially preserved in the shallower rhyolite intersections. These textures along with immediately overlying phreatomagmatic tuffs (see below) suggest emplacement as surficial domes and lava flows. By contrast, deeper rhyolites lack these textures, are more coarsely crystalline, and are consequently interpreted as small, subvolcanic intrusives.

Overlying the massive rhyolites in the shallow sections of wells Smith IW-2, Vulcan IW-8 and Elmore 16 are tuffaceous deposits with thicknesses of 10–30 m. These deposits comprise chaotically textured mixtures of sand- to silt-sized detrital grains (quartz, feldspar, lithic fragments) mingled with altered ash- to small lapilli-sized, vesicular pyroclasts that preserve textural characteristics of glass shards and pumice. Devitrified, dense rhyolitic clasts similar to the underlying massive rhyolite are also common in the tuffs. Hydrothermal alteration of these tuffaceous deposits is strong, with chlorite locally making up 30% of the rock.

A thin (1 m) layer of altered volcanic ash has been previously described from research well State 2-14 at a depth of 1,704 m (Fig. 2; Herzig and Elders, 1988), approximately equivalent to the depth where shallow subsurface rhyolites are encountered in SSGF wells, located ~5 km SW of State 2-14. Based on its rare-earth-element (REE) characteristics, this altered ash has been correlated with Bishop Tuff (Herzig and Elders, 1988). The presence of Bishop Tuff is also known from surface outcrops at the Durmid Hill, E of the Salton Sea, where steeply tilted, reworked distal Bishop ash can be laterally traced for several km (Izett et al., 1970) and locations in the NW part of the Salton Trough (Lutz et al., 2006). Because radiometric dates for the ash deposits at neither location, existed, we included surface and subsurface samples of the ash deposit in our present study (Table 1).

3. Methods

Zircons were extracted by heavy liquid separation from ~10–200 g of mm-sized drill cuttings colleted at ~3 m (10 ft) depth intervals from wells Smith IW-2, Vulcan IW-8 and Elmore 16. The cuttings were hand-crushed and sieved to a grain size <250 µm. In addition to cuttings, a cm-sized core from well State 2-14 and surface-sampled ash from Durmid Hill were disintegrated and processed in a similar fashion.

Due to the crystal-poor nature of the subsurface rhyolites, the yield of zircons was low and averaged only one zircon per 3 g of material processed. The actual yield of magmatic zircons was in many cases much lower because all samples were contaminated to variable extent by detrital zircons derived from sedimentary wall rocks fragments from up-section in the well, and no attempts were made to purify the cuttings before crushing. Zircons were hand-picked from the heavy-mineral fraction, and mounted in epoxy resin. Selected zircons with

Table 1
U–Pb results

Well/location	Name (depth in ft.)	Depth (m)	Grain	Spot	$^{238}U/^{206}Pb$ $\times 10^3$	± $\times 10^3$	$^{207}Pb/^{206}Pb$	±	cc	% radiogenic ^{206}Pb[a]	f	Age (ka)	± (Ka)	U (ppm)	Th (ppm)	$\delta^{18}O_{SMOW}$ (‰)	±	Remarks
Smith IW-2	5780	1762	1	1	17.2	0.3	0.163	0.015	0.16	85.1	1.29	411	10	4472	1989			Rim
	5780	1762	1	2	17.2	0.3	0.168	0.013	−0.17	84.4	1.29	409	9	3850	1718			Rim
	5780	1762	2	1	17.2	0.4	0.204	0.009	−0.02	79.8	1.31	391	9	4412	2026			Rim
	5780	1762	1	3	17.6	0.4	0.101	0.006	0.22	93.0	1.22	416	10	4963	4646	4.7	0.3	
	5780	1762	5	1	18.2	0.6	0.123	0.015	0.27	90.1	1.26	403	12	2270	1567			
	5780	1762	6	1	18.6	0.5	0.084	0.006	0.37	95.1	1.24	409	10	5412	4473			
	5780	1762	7	1	17.7	0.5	0.098	0.007	0.34	93.3	1.22	413	10	3864	3684			
	5780	1762	8	1	4.72	1.05	0.659	0.070	−0.05	21.7	1.27	375	415	3668	3010			
	5780	1762	9	1	9.35	0.20	0.479	0.012	0.12	44.6	1.27	392	19	3359	2290			
	5780	1762	10	1	18.1	0.5	0.098	0.009	−0.01	93.4	1.23	411	11	4604	3896			
	5780	1762	2	2	17.4	0.6	0.111	0.007	−0.21	91.8	1.22	416	13	3550	3208	5.0	0.3	
	5780	1762	11	1	18.5	0.5	0.106	0.009	0.34	92.4	1.24	398	10	3635	3299			
	5780	1762	12	1	19.3	0.6	0.079	0.010	0.03	95.8	1.28	409	20	6325	3379			
	5780	1762	13	1	14.1	0.8	0.325	0.037	0.12	64.3	1.30	380	33	1822	1085			
Smith IW 2 regression age (2σ age uncertainties): 420±8 ka (MSWD=1.8); weighted average of individual ages: 407±6 ka (MSWD=0.5)																		
Vulcan IW-8	6120	1865	1	1	15.7	1.3	0.171	0.030	0.36	84.1	1.26	434	38	411	234			
	6120	1865	3	1	10.9	1.6	0.543	0.076	0.02	36.5	1.41	303	117	273	153			
	6190	1887	1	1	12.2	0.4	0.164	0.024	0.07	85.0	1.20	537	23	848	458			[b]
	6190	1887	3	1	17.9	0.4	0.078	0.004	−0.17	95.9	1.22	421	11	5676	5102			
	6190	1887	4	1	2.93	0.14	0.644	0.035	−0.16	23.6	1.18	612	172	465	208			
	6190	1887	1	2	11.5	0.6	0.161	0.015	0.05	85.4	1.19	570	29	884	466			[b]
	6320	1926	1	1	16.1	1.4	0.233	0.053	0.37	76.1	1.29	393	43	267	159			
	6320	1926	2	2	2.48	0.39	0.667	0.056	−0.01	20.6	1.17	628	555	359	160			
	6320	1926	3	1	12.5	1.0	0.150	0.026	−0.21	86.7	1.20	536	45	514	272			[b]
	6320	1926	4	1	4.00	0.24	0.650	0.029	−0.04	22.9	1.21	448	137	6627	5444			
	6320	1926	5	1	1.17	0.05	0.758	0.035	0.03	9.0	1.20	597	410	974	261			
	6550	1996	8	1	11.1	0.6	0.372	0.010	0.05	58.3	1.22	415	34	5318	4941			
	6570	2003	1	1	6.93	0.57	0.290	0.061	0.51	68.9	1.13	724	97	319	220	5.3	0.3	[b]
	6570	2003	2	1	13.2	1.3	0.217	0.078	−0.57	78.1	1.23	470	72	1539	907	4.9	0.3	
	6570	2003	3	1	17.7	0.8	0.112	0.011	0.21	91.6	1.22	406	20	3200	3188	5.5	0.3	
	6570	2003	4	1	20.1	0.9	0.079	0.013	0.43	95.8	1.25	383	19	3878	3406	5.8	0.3	
	6570	2003	5	1	21.1	0.8	0.107	0.017	−0.20	92.2	1.29	364	18	3186	2299	6.3	0.3	
	6570	2003	6	1	19.9	1.5	0.159	0.035	−0.18	85.6	1.29	357	29	1042	820			
	6570	2003	7	1	8.14	0.44	0.340	0.031	−0.21	62.4	1.18	584	58	1319	712			[b]
	6570	2003	8	1	15.5	0.7	0.106	0.027	0.56	92.3	1.24	474	23	1510	737			
	6880	2097	1	1	14.0	0.8	0.366	0.041	0.17	59.2	1.38	375	34	3355	577			
	6880	2097	2	1	7.86	0.69	0.538	0.040	0.27	37.2	1.34	408	85	3181	541			
Vulcan IW 8 6120–6880 regression age (2σ age uncertainties): 433±19 ka (MSWD=2.6); weighted average of individual ages: 407±16 ka (MSWD=1.6)																		
Vulcan IW-8	8660	2640	3	1	12.1	0.6	0.294	0.027	0.10	68.3	1.26	460	33	835	320			
	8660	2640	3	2	12.5	0.7	0.391	0.030	−0.19	55.9	1.34	386	40	915	260			
	8660	2640	3	3	14.3	1.0	0.165	0.029	−0.05	84.8	1.24	473	36	614	306			
	8710	2655	1	1	18.6	1.0	0.096	0.013	0.03	93.6	1.26	408	19	939	656			
	8710	2655	2	1	10.0	0.6	0.472	0.032	0.33	45.6	1.29	378	47	574	384			
	8710	2655	5	1	14.3	0.8	0.106	0.018	0.16	92.4	1.23	510	26	1272	498	4.2	0.2	[b]
	8710	2655	8	1	3.37	0.18	0.697	0.037	0.11	16.8	1.28	409	150	637	362			
	8710	2655	9	1	15.6	1.5	0.134	0.041	0.09	88.8	1.24	457	45	223	120	3.6	0.2	
	8730	2661	1	1	18.8	1.5	0.189	0.050	0.04	81.7	1.31	366	34	733	453	3.9	0.3	
	8730	2661	2	1	17.2	1.8	0.255	0.050	0.19	73.3	1.31	359	46	357	230			
Vulcan IW 8 8660–8730 regression age (2σ age uncertainties): 424±28 ka (MSWD=1.7); weighted average of individual ages: 413±26 ka (MSWD=1.3)																		
Elmore 16	5160	1573	1	1	19.2	0.8	0.066	0.005	0.11	97.5	1.24	407	16	9625	7705			
	5160	1573	2	1	21.0	0.9	0.083	0.017	−0.17	95.3	1.22	357	14	6632	7883	4.4	0.2	
	5160	1573	3	1	10.3	1.2	0.424	0.055	−0.27	51.7	1.27	410	99	861	501	4.4	0.2	
	5160	1573	4	1	11.0	1.8	0.381	0.094	−0.38	57.2	1.27	425	139	1202	636	4.0	0.2	
	5160	1573	5	1	9.81	1.33	0.381	0.101	−0.16	57.2	1.24	465	131	628	339	4.5	0.2	
	5160	1573	6	1	5.05	0.42	0.589	0.088	0.13	30.6	1.24	486	178	89	34			
	5160	1573	1	1	13.0	0.6	0.257	0.014	0.13	73.0	1.20	435	27	7612	7769			
	5160	1573	5	1	16.2	0.9	0.159	0.012	−0.01	85.5	1.18	402	23	6426	8384			
	5160	1573	2	1	14.4	1.1	0.211	0.017	0.18	78.9	1.22	429	35	3152	2798			
	5160	1573	10	1	11.7	0.6	0.298	0.008	−0.08	67.8	1.18	439	33	9966	11871			
Elmore 16 5160–5190 regression age (2σ age uncertainties): 437±21 ka (MSWD=1.9); weighted average of individual ages: 396±20 ka (MSWD=1.5)																		
Elmore 16	6520	1987	1	1	9.12	0.57	0.518	0.043	−0.06	39.7	1.33	372	65	893	438	5.1	0.3	
	6520	1987	2	1	9.26	0.47	0.308	0.022	−0.09	66.5	1.19	553	43	1382	722			
	6520	1987	3	1	6.76	0.56	0.530	0.059	−0.25	38.2	1.24	451	127	282	171	4.5	0.3	
	6520	1987	4	1	12.2	0.6	0.321	0.031	0.40	64.8	1.26	430	31	1345	774	4.4	0.3	
	6520	1987	5	1	10.9	1.0	0.505	0.042	−0.10	41.3	1.33	325	75	638	487	4.6	0.3	
	6520	1987	6	1	8.55	0.67	0.344	0.031	0.17	61.9	1.18	549	67	754	539	4.7	0.3	
	6520	1987	7	1	9.61	0.55	0.366	0.031	0.18	59.2	1.23	488	47	877	432	4.8	0.3	
	6520	1987	4	2	3.94	0.55	0.662	0.048	0.00	21.2	1.27	442	310	822	342	4.0	0.3	

(continued on next page)

Table 1 (*continued*)

Well/location	Name (depth in ft.)	Depth (m)	Grain	Spot	$^{238}U/^{206}Pb$ $\times 10^3$	± $\times 10^3$	$^{207}Pb/^{206}Pb$	±	cc	% radiogenic ^{206}Pb[a]	f	Age (ka)	± (Ka)	U (ppm)	Th (ppm)	$\delta^{18}O_{SMOW}$ (‰)	±	Remarks
Elmore 16	6520	1987	3	2	5.41	0.63	0.729	0.095	0.11	12.7	1.56	235	217	310	209	4.8	0.3	
	6520	1987	1	1	7.11	0.21	0.337	0.014	−0.06	62.8	1.15	658	34	7583	4421			[b]
	6520	1987	5	1	5.96	0.24	0.454	0.023	0.05	47.8	1.18	609	57	801	379			[b]
	6520	1987	4	1	1.63	0.10	0.695	0.049	−0.23	17.1	1.12	756	449	883	705			
	6520	1987	1	2	8.19	0.13	0.164	0.006	−0.11	84.9	1.03	690	14	12828	30384			[b]
	6600	2012	1	1	15.4	1.0	0.097	0.016	0.24	93.4	1.24	484	28	725	338	4.9	0.2	
	6600	2012	1	1	16.3	1.4	0.151	0.023	0.19	86.5	1.27	435	36	621	278			
	6600	2012	1	2	16.9	1.2	0.106	0.022	0.01	92.3	1.25	440	29	755	427			
	6740	2054	2	1	13.0	1.0	0.263	0.025	0.25	72.3	1.24	443	40	1647	1085			
Elmore 16 6520–6740 regression age (2σ age uncertainties): 479±38 ka (MSWD=2.7); weighted average of individual ages: 457±28 ka (MSWD=1.2)																		
Elmore 16	7460	2274	1	1	18.6	0.9	0.090	0.008	−0.01	94.4	1.28	416	16	4532	2432	3.8	0.2	
	7460	2274	2	1	17.8	1.2	0.143	0.020	0.08	87.6	1.26	400	26	575	404	4.5	0.2	
	7460	2274	4	1	18.8	1.1	0.102	0.015	−0.18	92.9	1.25	398	22	1144	923	4.8	0.2	
	7460	2274	5	1	1.73	0.10	0.756	0.025	0.00	9.2	1.26	432	315	339	184	4.0	0.2	
	7460	2274	6	1	16.8	1.5	0.176	0.031	0.13	83.4	1.27	407	37	406	258			
	7460	2274	11	1	3.81	0.18	0.607	0.025	0.22	28.3	1.19	570	102	782	389			
	7460	2274	12	1	16.7	1.2	0.138	0.028	0.24	88.3	1.24	425	30	564	396	5.0	0.2	
Elmore 16 7460 regression age (2σ age uncertainties): 440±35 ka (MSWD=1.5); weighted average of individual ages: 411±20 ka (MSWD=0.5)																		
Durmid Hill (N 33°22'28'', W 115°46'07'')		Surface	1	1	8.65	0.53	0.071	0.005	0.08	96.8	1.12	808	46	3206	1798			
		Surface	2	1	9.00	0.23	0.057	0.004	0.10	98.5	1.12	791	44	3919	2316			
		Surface	3	1	8.80	0.21	0.064	0.004	0.16	97.7	1.12	803	45	2625	1407			
		Surface	4	1	9.08	0.20	0.066	0.004	−0.04	97.5	1.13	781	43	3697	1842			
		Surface	5	1	8.55	0.21	0.074	0.007	0.03	96.4	1.11	804	45	4599	3697			
		Surface	6	1	8.78	0.26	0.082	0.011	−0.12	95.4	1.13	791	44	2360	1092			
		Surface	7	1	8.79	0.20	0.066	0.004	0.23	97.4	1.12	800	44	4272	2517			
		Surface	8	1	8.73	0.27	0.104	0.015	−0.35	92.6	1.13	769	43	2953	1745			
		Surface	9	1	8.50	0.15	0.060	0.005	−0.13	98.2	1.11	826	46	4772	3210			
		Surface	10	1	9.16	0.18	0.060	0.004	−0.08	98.2	1.13	778	43	4236	2340			
		Surface	11	1	8.34	0.23	0.081	0.005	0.50	95.6	1.12	825	46	4142	2388			
		Surface	12	1	9.43	0.20	0.074	0.004	−0.08	96.4	1.13	746	41	3220	1808			
		Surface	13	1	6.56	0.17	0.284	0.010	0.38	69.6	1.12	768	43	3893	2472			
		Surface	14	1	8.61	0.29	0.112	0.010	0.16	91.6	1.14	778	43	1277	512			
		Surface	15	1	8.92	0.21	0.074	0.005	−0.12	96.4	1.13	785	44	3195	1644			
State 2-14		1704 m	36	1	7.81	0.36	0.188	0.018	−0.03	81.8	1.13	763	43	3566	1981			
		1704 m	36	2	8.24	0.54	0.198	0.022	−0.24	80.6	1.14	720	58	2839	1375			
		1704 m	36	3	7.83	0.49	0.166	0.026	−0.37	84.7	1.13	789	61	3223	1392			After repolishing
		1704 m	36	4	2.82	0.18	0.566	0.041	0.17	33.5	1.12	855	193	3571	1900			After repolishing
		1704 m	36	5	5.60	0.35	0.357	0.024	0.32	60.3	1.13	785	80	2907	1276			After repolishing
Bishop tuff regression age (2σ age uncertainties): 802±12 ka (MSWD=1.7); weighted average of individual ages: 784±22 ka (MSWD=0.26)																		
Xenocrysts					$\times 10^0$	$\times 10^0$						(Ma)	(Ma)					
Smith IW 2	5780	1762	4	1	294	6	0.062	0.004	−0.05	98.0	1.00	21.6	0.4	389	182			Rim
	5780	1762	3	1	321	11	0.106	0.012	−0.26	92.3	1.01	18.6	0.8	580	184			Rim
	5780	1762	3	2	318	6	0.053	0.003	−0.13	99.1	1.00	20.1	0.5	352	187			
	5780	1762	4	2	319	8	0.048	0.001	0.25	99.7	1.00	20.2	0.5	1008	438			
Vulcan IW 8	6500	1981	1	1	298	8	0.098	0.008	−0.34	93.3	1.00	20.2	0.6	382	166			Rim
	6500	1981	1	2	316	8	0.058	0.003	−0.12	98.5	1.00	20.2	0.5	367	148			
	6500	1981	2	1	332	6	0.059	0.004	−0.24	98.3	1.00	19.2	0.4	413	175			Rim
	6500	1981	2	2	293	10	0.067	0.007	−0.16	97.3	1.00	21.5	0.8	190	85			
	6500	1981	3	1	292	6	0.065	0.006	−0.02	97.7	1.00	21.6	0.5	272	122			Rim
	6500	1981	3	2	280	5	0.113	0.003	0.01	91.5	1.00	21.1	0.5	395	157			
	8730	2661	2	1	2.57	0.08	0.129	0.001	−0.05	100.1	1.00	2122	103	149	126	9.7	0.3	
	8730	2661	3	1	20.2	0.5	0.054	0.001	−0.10	99.8	1.00	311	15	330	373	6.1	0.3	
	8730	2661	4	1	66.5	1.5	0.049	0.002	0.23	99.9	1.00	96.2	4.7	533	261	8.4	0.3	
	8710	2655	6	1	119	6	0.045	0.002	0.06	100.2	1.00	54	3	517	328	6.8	0.2	
Elmore 16	7460	2274	3	1	5.04	0.38	0.078	0.001	0.01	100.1	1.00	1168	80	61	30	7.7	0.2	

Geothermal well sample naming based on sampled depth interval (10 ft).
Individual spot uncertainties quoted at 1σ level; average age uncertainties as 2σ errors.
cc error correlation coefficient.
f ^{230}Th disequilibrium correction factor calculated from $(Th/U)_{zircon}/(Th/U)_{melt}$ assuming $(Th/U)_{melt}=3.1$[a](Herzig and Elders, 1988) and 2.81[b](Crowley et al., 2007).

[a] ^{207}Pb corrected using common Pb compositions: $^{206}Pb/^{204}Pb=18.86$; $^{207}Pb/^{204}Pb=15.62$.

[b] Excluded from age regression.

crystal faces oriented flush to the epoxy surface were first analyzed without grinding and polishing ("rim" analyses). The mounts were subsequently ground and polished to expose crystal interiors ("core" analyses). Images in backscatter and cathodoluminescence (CL) modes were generated from the zircons using a Leo VP 1430 scanning electron microprobe (Fig. 3).

Zircon U–Pb analyses were conducted using the Cameca ims 1270 ion microprobe at the University of California Los Angeles, using standard zircon AS3 (Paces and Miller, 1993), and following protocols in Schmitt et al. (2003). $^{206}Pb/^{238}U$ zircon-model ages were calculated from the intercepts of a linear regression "fixed" to anthropogenic common Pb with $^{207}Pb/^{206}Pb=0.823$ (Sanudo-Wilhelmy and Flegal, 1994) with a modified "Concordia" curve where $^{207}Pb/^{206}Pb$ and $^{238}U/^{206}Pb$ coordinates were calculated accounting for initial disequilibrium in long-lived U-series intermediate daughter products. Salton Sea subsurface rhyolite zircons are too old to directly measure disequilibrium, and therefore initial disequilibrium was estimated from surface rhyolite data that yielded Th/U and Pa/U zircon-melt partitioning ratios of 0.2 and 2, respectively (Schmitt, 2007). Uncertainties in zircon-melt partitioning ratios as well as U-series disequilibria of melt and other intermediate isotopes besides ^{230}Th and ^{231}Pa will cumulatively amount to additional age uncertainties <10 ka, and are therefore negligible compared to measurement uncertainties. Similarly, uncertainties in common $^{207}Pb/^{206}Pb$ and decay constants are unaccounted for, because these effects are significantly smaller than measurement uncertainties. Individual disequilibrium-corrected zircon $^{206}Pb/^{238}U$ model ages were calculated using a ^{207}Pb-based correction. The averages for $^{206}Pb/^{238}U$ model ages overlap within uncertainties with the regressions ages (Table 1).

A subset of zircon crystals was reground and polished to remove all traces from sputter pits that became contaminated by the mass-filtered ^{16}O negative ion beam used in U–Pb analysis and subsequently analyzed for $^{18}O/^{16}O$ isotopes following the methods outlined in Trail et al. (2007). Oxygen isotopic values are reported as $\delta^{18}O_{SMOW}$ using AS3 or Pacoima reference zircons (Booth et al., 2005; Trail et al., 2007) to correct for instrumental mass fractionation. During the analytical sessions, accuracy and precision of the instrumental mass fractionation was monitored by analyzing the 91,500 reference zircon (Valley, 2003) on the same mounts. Based on the results for 91,500 (June 25, 2005: $\delta^{18}O=9.76\pm0.27$‰, 1 standard deviation, $n=6$; October 26, 2007: $\delta^{18}O=9.46\pm0.19$‰, $n=7$; November 21 2007: $\delta^{18}O=10.25\pm0.39$‰, $n=11$), we estimate both accuracy and precision to be about ± 0.2–0.3‰ (1σ) for individual analysis spots, compared to the bulk composition of 91,500 zircon of $\delta^{18}O=9.86$‰ (Valley, 2003). We also report whole-rock Sr, Nd, and Pb isotopic data that were analyzed from hand-picked rhyolite cuttings by Geochron Laboratories (Krueger Enterprises, Inc).

4. Results

4.1. Subsurface rhyolites

From a total of 19 processed rhyolite cutting samples, 15 yielded zircons with Pleistocene $^{206}Pb/^{238}U$ zircon ages (Fig. 4; Table 1). The Pleistocene zircon population shows age heterogeneity, whereby ~10% of the zircons predate the dominant population by up to ~300 ka. We excluded these "antecrysts" (zircon from earlier episodes of a long-lived magmatic event) from the calculation of average zircon crystallization ages, but will discuss their significance below. Because zircon ages for multiple samples from a coherent rhyolite intersection are homogeneous, we combined all results from individual rhyolite intersections to calculate an average age (Table 1, Fig. 4).

The shallowest rhyolite intersections in wells Smith IW-2, Vulcan IW-8 and Elmore 16 yield overlapping concordia intercept ages of 420 ± 8 ka, 433 ± 19, and 437 ± 21 ka, respectively (2σ uncertainties multiplied by square-root of MSWD to account for excess scatter). Results for two intrusive rhyolites in wells Vulcan IW-8 and Elmore 16 overlap, with ages of 424 ± 28 ka and 440 ± 35 ka, respectively. Zircons from the deeper extrusive rhyolite sample Elmore 16 6520–6740 (average 479 ± 38 ka) are older than those of the overlying Elmore 16 5160–5190, with an age difference of 42 ± 35 ka (2σ). Although this age difference is only marginally resolved, average zircon U abundances are noticeably higher in the younger rhyolites (~3700 ppm compared to ~850 ppm; Fig. 4), supporting age and petrographic indications that two separate extrusive events are recorded in well Elmore 16.

Oxygen-isotopes in SSGF late Pleistocene zircons average $\delta^{18}O=4.6$‰ (±0.6‰ 1 standard deviation; Table 1; Fig. 5). By contrast, $\delta^{18}O$ values in pre-Pleistocene zircons are typically higher, with values between 6.1 and 9.7‰ (Table 1; Fig. 5). Whole-rock Sr, Nd, and Pb isotopic compositions are summarized in Table 2 and Fig. 6. $^{87}Sr/^{86}Sr$ ratios range between 0.7112 and 0.7114. These values are only slightly lower than those of metasedimentary rocks from the State 2-14 well (0.713; Herzig and Elders, 1988; Herzig and Jacobs, 1994). Epsilon Nd values of the subsurface rhyolites (average $\varepsilon Nd=+4.0$), by contrast, are clearly higher compared to sedimentary ($\varepsilon Nd=-10$ to -11) or batholitic basement rocks ($\varepsilon Nd=-8.5$; Herzig and Jacobs, 1994), and can be reconciled with dominantly mid-oceanic ridge-type mantle origins with minor (~10%) crustal contamination by mixing or assimilation (Fig. 6).

4.2. Zircon antecrysts and absence of intra-grain age zonation

The cumulative probability curves for Pleistocene zircons display prominent peaks at ~400–450 ka which tail off to ages as old as ~700 ka (Fig. 4). Based on CL textures, we were not able to distinguish

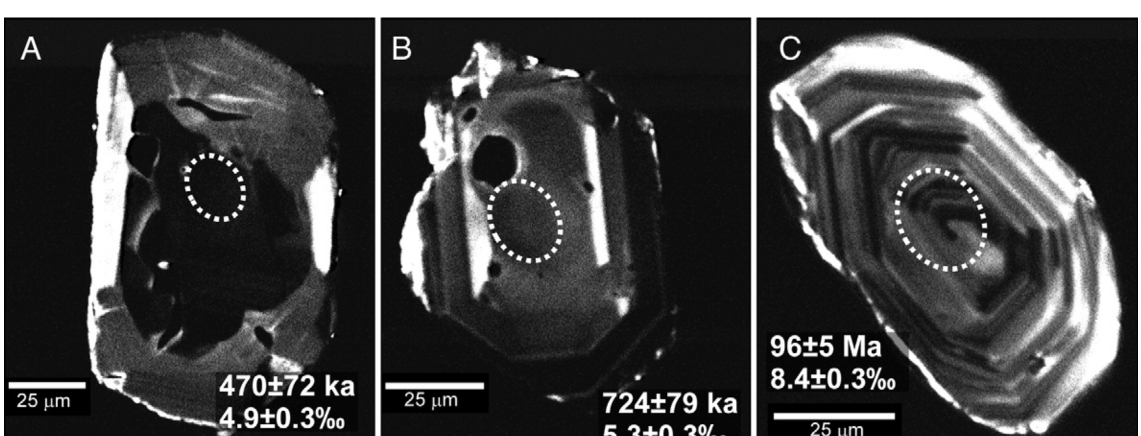

Fig. 3. Selected cathodoluminescence (CL) images of zircons from Salton Sea subsurface rhyolites. $^{206}Pb/^{238}U$ model ages and oxygen isotopic compositions are presented (individual analysis errors 1σ). Note that age analysis spots are only approximate due to regrinding and repolishing subsequent to U–Pb analysis and before oxygen isotopic analysis. (A) Vulcan IW-8 6570' g2; (B) Vulcan IW-8 6570' g1; (C) Vulcan IW-8 8730' g4.

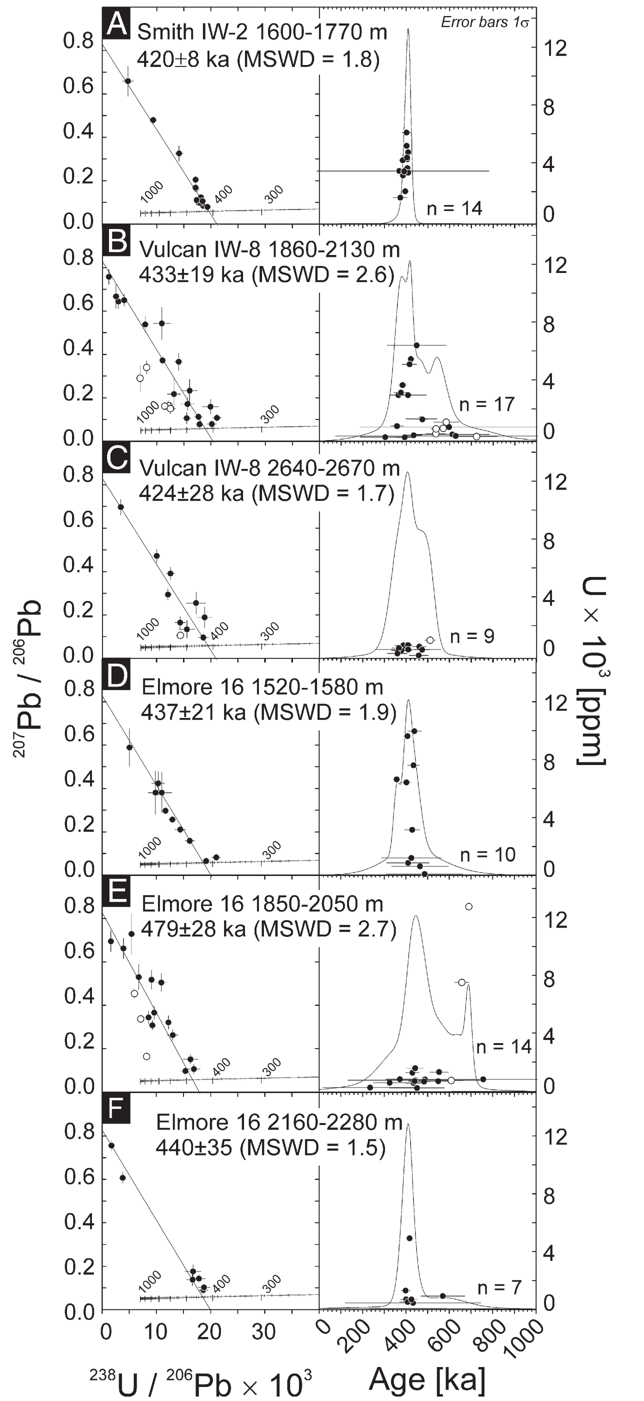

Fig. 4. ^{207}Pb/^{206}Pb vs. ^{238}U/^{206}Pb isochron diagram showing zircon results from SSGF subsurface samples. Ages are regression ages from intersection of the fixed-intercept (common ^{207}Pb/^{206}Pb = 0.82; Sanudo-Wilhelmy and Flegal, 1994) regression line with concordia modified for initial U-series disequilibrium (see text). Data used for regression are indicated with solid symbols, whereas open symbols are interpreted as antecrysts that are excluded from the regression. Probability density curves (right panels) are calculated from individual ^{207}Pb-corrected ^{206}Pb/^{238}U zircon ages that are plotted against zircon U abundance. Age uncertainties are quoted at 2σ level.

older zircon antecrysts from the dominant younger population (Fig. 3A and B). However, the Pleistocene zircons have characteristically lower CL activity and less prominent oscillatory banding compared to pre-Pleistocene zircons (Fig. 3C) that cover similar age ranges as detrital zircons from well State 2–14, and thus are likely derived from the sedimentary wall rocks. Replicate U–Pb analyses of zircon antecrysts reproduce within uncertainty, and suggest age homogeneity of the antecrysts within the ~25 µm lateral spatial resolution of the ion microprobe spot.

We also made an effort to check for potential hydrothermal zircon overgrowth that would go undetected in conventional spot analysis mode by analyzing unadulterated crystal faces (rims) in depth profiling mode (Reid and Coath, 2000). In this mode, spatial resolution of ion microprobe analysis across zircon growth domains is enhanced by at least a factor of 50. Subsequently, we analyzed the interiors of the same crystals in conventional spot mode following grinding and polishing. Both for late Pleistocene and detrital zircon crystals, rim and core ages reproduced within uncertainty, suggesting a complete lack of zircon (re-)crystallization during hydrothermal alteration (Fig. 7).

4.3. Bishop Tuff

Bishop Tuff zircons from the Durmid Hill surface outcrop are frequently mantled by adherent volcanic glass, and therefore are easily overlooked in hand-picking. From visual inspection of the heavy-mineral separate and laser ablation inductively coupled plasma mass spectrometry (LA-ICPMS) dating of zircons from the Durmid Hill ash (Schmitt, unpublished data), we estimate that ~90% of the zircons are detrital, although this may be biased due to less effective settling of glass-coated Bishop Tuff zircons during heavy liquid separation. U–Pb ages and U concentrations of Durmid Hill zircons (Fig. 8) agree excellently with published bulk (Crowley et al., 2007) and ion microprobe (Reid and Coath, 2000; Simon and Reid, 2005) data for Bishop Tuff and confirm previous tephrostratigraphic correlations of the Durmid Hill ash with Bishop Tuff (Izett et al., 1970).

The State 2-14 core sample (1704 m depth) has been previously identified as distal Bishop Tuff based on REE and trace element characteristics. We analyzed ~80 zircons extracted from a piece of drill core from 1704 m depth, and found three Quaternary zircon crystals (one by ion microprobe analysis; Table 1; two by LA-ICP MS; Schmitt, unpublished data) for which U–Pb ages agree closely with the ages for Bishop Tuff zircons (Fig. 8). It should be noted that the dominantly detrital zircon population found in the State 2-14 core sample is consistent with the reworked nature of Bishop ash at the Durmid Hill surface outcrop.

5. Discussion

5.1. Timing and origins of Salton Sea rhyolite volcanism

The results presented here provide the first evidence for rhyolitic volcanism in the Salton Trough during the Pleistocene. Previous estimates for the age of subsurface rhyolites (Hulen and Pulka, 2001) were based on extrapolation of sedimentation rates constrained by the presence of Bishop ash in well State 2-14 at 1704 m depth, but U–Pb zircon crystallization ages between ~420 and 470 ka demonstrate that extrapolated ages are overestimated by >350 ka. Diffusive Pb loss at temperatures of 200–300 °C (or higher) is insignificant, and the absence of hydrothermal zircon dissolution and re-precipitation is demonstrated by concordant rim and core analyses of Pleistocene and detrital zircons at a few 100 nm depth resolution (Fig. 7). These results underline the outstanding property of zircon to reliably record

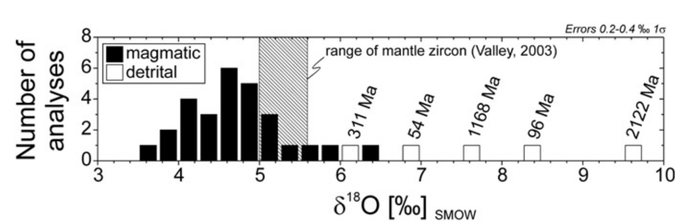

Fig. 5. Zircon oxygen isotopic compositions for SSGF subsurface rhyolites.

Table 2
Whole-rock Sr, Nd and Pb isotopic results

Well	Name (depth in ft)	Depth (m)	$^{87}Sr/^{86}Sr$	±	$^{143}Nd/^{144}Nd$	±	$^{206}Pb/^{204}Pb$	$^{207}Pb/^{204}Pb$	$^{208}Pb/^{204}Pb$
Smith IW 2	5600–5620	1707–1713	0.711262	0.000010	0.512833	0.000008	19.040	15.646	38.868
Vulcan IW 8	6300–6320	1920–1926	0.711342	0.000007	0.512839	0.000006	18.945	15.641	38.558
Vulcan IW 8	6700–6720	2042–2048	0.711314	0.000006	0.512851	0.000004	19.048	15.646	38.793
Vulcan IW 8	6850–6860	2088–2091	0.711077	0.000008	0.512846	0.000006	18.931	15.669	38.550
Elmore 16	6540–6560	1993–1999	0.711397	0.000011	0.512839	0.000007	19.130	15.657	38.969
Elmore 16	7440–7460	2268–2274	0.711343	0.000009	0.512838	0.000005	19.105	15.652	38.931

Uncertainties quoted as 2σ standard deviations; precision of Pb isotopic ratios better than 0.1%.

crystallization ages even under conditions of high ambient temperatures and fluid flow that caused replacement of essentially all other primary phases in these rhyolites during propylitic to potassic hydrothermal alteration.

Because of the strong alteration of the subsurface rhyolites, only fluid-immobile geochemical tracers (oxygen-isotopes in zircon and Nd-isotopes) reliably constrain the origins of the SSGF subsurface rhyolites. We deem Pb- and Sr-isotopes unreliable to record magmatic compositions due to the intense alteration and recrystallization of feldspars, and exchange with sedimentary sources via hydrothermal fluids. Whole-rock Nd isotopic compositions indicate mantle-like compositions for the rhyolite magmas. This allows the SSGF rhyolites to be clearly distinguished from crustally derived melts which would inherit low εNd of the regional (meta-)sedimentary or granitic source rocks (Fig. 6). Elevated εNd of subsurface and surface rhyolites (and basaltic xenoliths) between +3.8 and +8.4 is indicative of a depleted MORB-type source of the basaltic parental magmas (Fig. 5). In this context, the presence of partially molten amphibole-bearing basalt xenoliths in Salton Buttes lavas is a key observation that demonstrates the viability of deriving high-silica rhyolites by low-pressure melting of hydrated basalts (Robinson et al., 1976). Zircon oxygen-isotopic compositions, after correcting for ~1‰ zircon-melt oxygen-isotopic fractionation at magmatic temperatures (Valley, 2003), indicate magma compositions similar to mantle, and are in general lower than expected for rhyolitic residual melt generated by fractional crystallization of basalt (Valley, 2003). This requires significant addition of a low-δ^{18}O meteoric water component, likely via deep-reaching convection of hydrothermal fluids that altered young MORB-type basaltic crust. Subsequent remelting of such hydrothermally altered, hydrated gabbros by magma recharge can generate SiO_2-rich melts (e.g., Spulber and Rutherford, 1983; Koepke et al., 2007). Low-δ^{18}O zircons from surface rhyolites and xenoliths (Schmitt and Vazquez, 2006) share these characteristics.

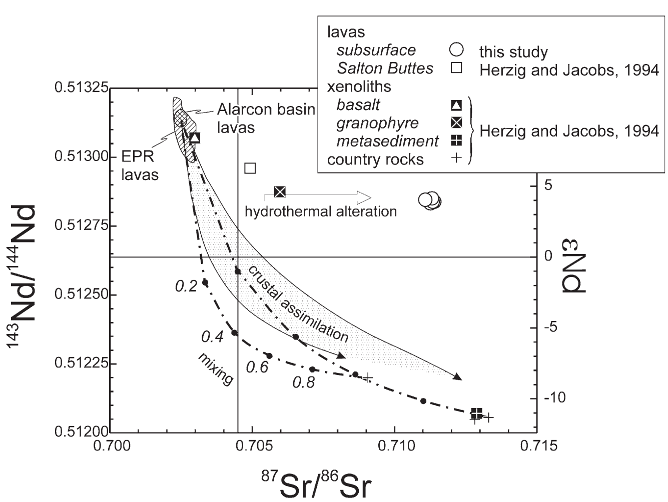

Fig. 6. Nd vs. Sr isotopic compositions for SSGF subsurface rhyolites. Other symbols are for surface rhyolites, xenoliths, and regional crustal rocks (Herzig and Jacobs, 1994). Hatched fields indicate compositions for oceanic lavas from the Alarcon basin and East Pacific Rise (EPR; Castillo et al., 2002 and references therein). Mixing and assimiliation—fractional crystallization (AFC) lines for Alarcon-type basaltic parental magma (Castillo et al., 2002) and two contrasting crustal end-members (AFC parmeters are: $D_{Nd}=0.3$, $D_{Sr}=1.8$, end points of curves for fraction of remaining melt $F=0.5$, rates of assimilation over crystallization between $r=0.1$ and 0.9).

5.2. Well stratigraphy and sedimentation rates

Pre-eruptive zircon crystallization is widely recognized, e.g., in Inyo Domes rhyolites (California) where zircon U–Th ages exceed the eruption age by 100 ka or more (Reid et al., 1997). U–Th zircon ages of Salton Buttes rhyolites, by contrast, have a more restricted age range between ~18 and 10 ka (Schmitt and Vazquez, 2006). The eruption age of the Salton Buttes is poorly constrained, but is likely Holocene. Zircon crystallization ages thus could overestimate the eruption age by ~10–20 ka.

A second concern for using zircon crystallization ages as a proxy for the eruption age is the presence of antecrysts. Again, a comparison of the subsurface rhyolite results with the Salton Buttes rhyolites is instructive: surface lavas contain granophyric xenoliths that yielded zircon crystallization ages of ~20 ka. It is therefore conceivable that the subsurface lavas may also have scavenged zircons from intrusions that became emplaced piecemeal prior to the eruption. This is also similar to results for Devils Kitchen rhyolite at Coso where zircon antecrysts predate the dominant zircon population with near-eruption ages by up to 200 ka (Miller and Wooden, 2004). For the subsurface rhyolites, a small proportion of the zircons predate the dominant population by several 100 ka, but a younger age peak can clearly be discerned and interpreted as near-eruption age based on the comparison with SSGF surface rhyolites.

Our textural interpretation of the shallow rhyolite intersection in wells Smith IW-2, Vulcan IW-8 and Elmore 16 as extrusive is supported by the slightly older age of the underlying rhyolite intersection in well Elmore 16. The deeper intrusive rhyolites in

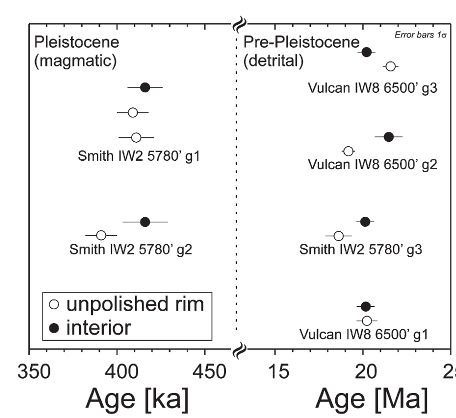

Fig. 7. Age results for replicate analyses on unpolished crystal surfaces and crystal interiors after grinding and polishing. Depths of individual analysis craters are ~500 nm.

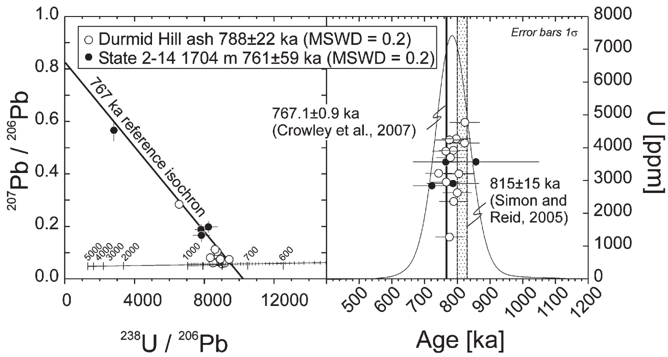

Fig. 8. ^{207}Pb/^{206}Pb vs. ^{238}U/^{206}Pb isochron diagram showing zircon results for Durmid Hill ash sample (open symbols) and State 2-14 altered ash at 1704 m depth (solid symbols). Weighted average ages after ^{207}Pb-based correction and disequilibrium correction agree within uncertainties (quoted at 2σ level) with published ages for Bishop Tuff (Reid and Coath, 2000; Simon and Reid, 2005; Crowley et al., 2007).

wells Vulcan IW-8 and Elmore 16, by contrast, are indistinguishable in age from the shallow rhyolites, and consequently are interpreted as coeval subvolcanic sills.

The buried extrusive rhyolites in the SSGF represent valuable surface markers in the sedimentary succession of the Salton Trough. Their lateral extent within the SSGF subsurface remains to be evaluated once information from further drilling becomes available. Rhyolitic lavas, however, are conspicuously absent in well State 2-14 and neighboring, newly completed CHAR (LLC) production well Hudson-13-1, roughly 5 km NNE of the SSGF geothermal wells. This suggests a relatively restricted horizontal extent of the subsurface lavas, similar to the surficial Salton Buttes domes and lava complexes that collectively extent over a ~0.8 km^2 area. Conversely, Bishop Tuff has not been found in wells Smith IW-2, Vulcan IW-8 and Elmore 16.

In the Salton Trough, subsidence is accompanied by rapid sedimentation so that near-sea level surface elevations are maintained (Lachenbruch et al., 1985). Using zircon U–Pb ages of SSGF subsurface rhyolites, the eruption age of Bishop Tuff (770 ka), and the depth at which both presently occur in geothermal wells, we thus can calculate average sedimentation rates that closely approximate subsidence rates. Our data indicate a twofold accelerated subsidence towards the center of the Salton Trough. For well Smith IW-2, the sedimentation rate averaged over the past 420 ka is 3.8±0.1 mm/a, nearly twice the rate constrained by Bishop Tuff in well State 2-14 (2.2±0.02 mm/a). Rapid subsidence in the center of the Salton Trough during the late Pleistocene and Holocene also contrasts with results from the NW Salton Trough where subsidence ceased by ~0.6 Ma (Lutz et al., 2006; Kirby et al., 2007).

Subsidence rate estimates based on subsurface rhyolite zircon crystallization ages are minimum values given the possibility of pre-eruptive zircon crystallization. The tops of individual rhyolite intersections in SSGF wells vary unsystematically with distance from the trough center by several 100 m. This could reflect topographic variations at the time of rhyolite effusion, diachronous rhyolite eruptions with nearly coeval zircon crystallization ages, or post-depositional tectonic offsetting of a laterally coherent lava complex. In any case, the age differences between SSGF lavas and Bishop Tuff, as well as the absence of Bishop Tuff in the SSGF wells at depths equal to or deeper than in well State 2–14, provide evidence for increased sedimentation and subsidence rates towards the center of the trough, with near doubling of the subsidence rates over <5 km lateral distance.

5.3. Magmato-tectonic evolution of the SSGF

Measured regional subsidence rates of 3 mm/a (Larsen and Reilinger, 1991) and model subsidence rates calculated from modern slip rates along the San Andreas–Imperial fault systems for the central portion of Salton Trough between 4 and 8 mm/a (Smith and Sandwell, 2003) are in reasonable agreement with the long-term subsidence rates presented in this study. Rifting in the Gulf of California province occurs in segments with highly contrasting styles of extension and magmatism, ranging from nearly amagmatic, delocalized rifts to narrow rifts with very little foundered continental crust present (Elders et al., 1972; Oskin and Stock, 2003; Lizarralde et al., 2007). Narrow rift segments with high sedimentation in the Northern Gulf of California (e.g., the Guaymas basin) are characterized by significant addition of basaltic magmas via intrusion into the overlying sediments (Lizarralde et al., 2007). For the Salton Trough, Lachenbruch et al. (1985) modeled extension concomitant with subsidence, sedimentation and basaltic intrusion and calculated that significant crustal melting would occur if extension was localized in a narrow, oceanic ridge-type zone. Because seismic evidence for molten crust is absent, they concluded that extension in the Salton Trough is broadly distributed over a much wider zone (~150 km) than the localized zones of seismic activity (~25 km; Lachenbruch et al., 1985).

Our results show that the rhyolites in the SSGF subsurface preserve evidence for remelting of hydrothermally altered MORB-type crust, which requires temperatures of ~900 °C in order to produce 10% rhyolitic partial melt (Spulber and Rutherford, 1983). These remelting events occurred episodically over the past 400 ka, and were narrowly localized. At the same time, evidence for melting of continental crust or sediments is lacking for the Salton Trough, consistent with earlier findings by Robinson et al. (1976) and Herzig and Jacobs (1994). It is also conspicuous that the SSGF is characterized by a local seismic velocity high with >4 km/s velocity rocks at 2–3 km depth, which may reflect hydrothermal densification and high-temperature metamorphism of the sediments or multiple basaltic sills localized in a zone of recurrent intrusive magmatism and associated elevated heat flow (Fig. 1; Fuis and Kohler, 1984; Parsons and McCarthy, 1996).

Thermal modeling of borehole temperature profiles (Kasameyer et al., 1984), U-series isotopic dating of SSGF brines (Zukin et al., 1987), and thermochronology of reservoir sandstone K-feldspar (Heizler and Harrison, 1991) suggest that the shallow portion of the SSGF is a very recent feature, probably not older than few thousand years to 10s of ka. Present-day high heat flow in the SSGF may thus be a transient feature related to shallow intrusions predating and overlapping with Holocene Salton Buttes volcanism (Schmitt and Vazquez, 2006). Pleistocene rhyolitic volcanism within the SSGF, however, implies the existence of an earlier hydrothermal system that altered newly formed basaltic crust and possibly cooled the base of the sedimentary fill of the Trough, preventing extensive partial melting. While the aggregate thickness of felsic igneous rock in the drilled portion of the SSGF subsurface significantly exceeds that of mafic igneous rocks (Hulen et al., 2003), the predominance of extruded rhyolites and felsic intrusions in the shallow portion of the SSGF may be biased due to dense basaltic magmas stalling at depth. Mafic sills and intrusions ponding at greater depth could thus represent the main heat source for the SSGF (Elders et al., 1984; McKibben et al., 1988), similar to oceanic spreading centers with high sediment input such as in the Guaymas basin (Fisher and Becker, 1991). Alternatively, silicic intrusions (e.g., Hulen et al., 2002) extracted from partially re-molten basaltic crust are conceivable as a direct heat source for the SSGF. The latter scenario would be consistent with the presence of Pleistocene granophyric xenoliths in Salton Buttes lavas (Schmitt and Vazquez, 2006) and similar felsic plutonic rocks in other examples of continental rupture zones (e.g., Danakil Depression, Lowenstern et al., 1997).

In order to improve understanding of the thermal and magmatic evolution of the SSGF, tighter constraints on the nature of its host rocks at depths >3 km are needed. ~20 ka granophyric xenoliths in Holocene Salton Buttes rhyolites reveal that felsic intrusions exist at depths >3 km for which no effusive counterparts have been encountered. Moreover, the ages of basaltic sills penetrated by numerous SSGF wells are presently unknown, precluding constraints on the recurrence of basaltic intrusions. Finally, thermal consequences of deep crustal hydrothermal convection evident from low-δ^{18}O rhyolites and hydrated basaltic xenoliths remain poorly understood. Heat flow considerations that characterize the Salton Trough as a wide continental rift thus should be subjected to closer scrutiny.

6. Conclusions

(1) Rhyolite volcanism in the Salton Trough predates Holocene surficial lavas and domes by at least 400 ka, based on U–Pb zircon ages for buried rhyolites in the subsurface of the Salton Sea Geothermal Field (SSGF);
(2) Oxygen-isotopic compositions of SSGF zircons are significantly lower than mantle and continental crust or sedimentary values. This precludes partial melting of (meta-)sediments or granitic basement as the source of rhyolite volcanism, and requires melting of rocks that have isotopically exchanged with meteoric waters;
(3) Nd-isotopes indicate a close affinity between subsurface rhyolites and MORB, suggesting re-melting of juvenile, hydrothermally altered, basaltic crust as the source of the rhyolites;
(4) Accelerated subsidence towards the center of the Salton Trough is evident from the presence of 400 ka Pleistocene pyroclastics and lavas in the SSGF subsurface at depths equivalent to altered ash from the 770 ka Bishop Tuff eruption in well State 2–14. Subsidence rates in the Salton Sea vary between ~2 and ~4 mm/a over ~5 km lateral distance, requiring substantial vertical offsets by high-angle normal faulting;
(5) The present-day active geothermal field is a zone of localized episodic rhyolite volcanism, coupled with high heat flow, metamorphism, and basaltic intrusive activity. Although the modern geothermal anomaly is recent and likely related to Holocene volcanism, deep-reaching precursor hydrothermal systems must have already existed during the Pleistocene.

Acknowledgments

Thanks to Michelle Hopkins for assistance with sample preparation, and Janet C. Harvey for assistance in sampling Bishop ash at Durmid Hill. We thank journal reviewers and the editor for their contributions to improving this manuscript. CalEnergy Operating Co. is thanked for providing generous access to geothermal well cuttings. The ion microprobe facility at the UCLA is partly supported by a grant from the Instrumentation and Facilities Program, Division of Earth Sciences, National Science Foundation.

References

Bertani, R., 2005. World geothermal power generation in the period 2001–2005. Geothermics 34 (6), 651–690.
Booth, A.L., Kolodny, Y., Chamberlain, C.P., McWilliams, M., Schmitt, A.K., Wooden, J., 2005. Oxygen isotopic composition and U–Pb discordance in zircon. Geochimica et Cosmochimica Acta 69 (20), 4895–4905.
Castillo, P.R., Hawkins, J.W., Lonsdale, P.F., Hilton, D.R., Shaw, A.M., Glascock, M.D., 2002. Petrology of Alarcon Rise lavas, Gulf of California: Nascent intracontinental ocean crust. Journal of Geophysical Research-Solid Earth 107 (B10), 2222. doi:10.1029/2001JB000666.
Crowley, J.L., Schoene, B., Bowring, S.A., 2007. U–Pb dating of zircon in the Bishop Tuff at the millennial scale. Geology 35 (12), 1123–1126.
Dorsey, R.J., Fluette, A., McDougal, K., Housen, B.A., Janecke, S.U., Axen, G.J., Shirvell, C.A., 2007. Chronology of Miocene–Pliocene deposits at Split Mountain Gorge, Southern California; a record of regional tectonics and Colorado River evolution. Geology 35 (1), 57–60.
Elders, W.A., Rex, R.W., Meidav, T., Robinson, P.T., Biehler, S., 1972. Crustal spreading in Southern California. Science 178 (4056), 15–24.
Elders, W.A., Bird, D.K., Williams, A.E., Schiffman, P., 1984. Hydrothermal flow regime and magmatic heat source of the Cerro Prieto geothermal system, Baja California, Mexico. Geothermics 13 (1–2), 27–47.
Fisher, A.T., Becker, K., 1991. Heat flow, hydrothermal circulation and basalt intrusions in the Guaymas Basin, Gulf of California. Earth and Planetary Science Letters 103 (1–4), 84–99.
Fuis, G.S., Kohler, W.M., 1984. Crustal structure and tectonics of the Imperial Valley region, California. Field trip guidebook—Pacific section. Society of Economic Paleontologists and Mineralogists 40, 1–13.
Fuis, G.S., Mooney, W.D., Healy, J.H., McMechan, G.A., Lutter, W.J., 1984. A seismic refraction survey of the Imperial Valley region, California. JGR. Journal of Geophysical Research B 89 (2), 1165–1189.
Heizler, M.T., Harrison, T.M., 1991. The heating duration and provenance age of rocks in the Salton Sea geothermal field, Southern California. Journal of Volcanology and Geothermal Research 46 (1–2), 73–97.
Herzig, C.T., Elders, W.A., 1988. Nature and significance of igneous rocks cored in the State 2-14 research borehole—Salton-Sea-Scientific-Drilling-Project, California. Journal of Geophysical Research-Solid Earth and Planets 93 (B11), 13069–13080.
Herzig, C.T., Jacobs, D.C., 1994. Cenozoic volcanism and two-stage extension in the Salton Trough, Southern California and northern Baja California. Geology 22 (11), 991–994.
Hulen, J., Pulka, F.S., 2001. Newly-discovered, ancient extrusive rhyolite in the Salton Sea Geothermal Field, Imperial Valley, California. Proceedings, Twenty-Sixth Workshop on Geothermal Reservoir Engineering. Stanford University, Stanford, pp. 1–16.
Hulen, J.B., Kaspereit, D., Norton, D.L., Osborn, W., Pulka, E.S., 2002. Refined conceptual modeling and a new resource estimate for the Salton Sea geothermal field, Imperial Valley, California. Geothermal Resources Council, Transactions 26, 29–36.
Hulen, J.B., Norton, D., Kaspereit, D., Murray, L., van de Putte, T., Wright, T., 2003. Geology and a working conceptual model of the Obsidian Butte (Unit 6) Sector of the Salton Sea Geothermal Field, California. Geothermal Resources Council Transactions 27, 227–240.
Izett, G.A., Wilcox, R.E., Powers, H.A., Desborough, G.A., 1970. The Bishop ash bed, a Pleistocene marker bed in the western United States. Quaternary Research (New York) 1, 121–132.
Kasameyer, P.W., Younker, L.W., Hanson, J.M., 1984. Development and application of a hydrothermal model for the Salton Sea geothermal field, California. Geological Society of America Bulletin 95 (10), 1242–1252.
Kirby, S.M., Janecke, S.U., Dorsey, R.J., Housen, B.A., Langenheim, V.E., McDougall, K.A., Steely, A.N., 2007. Pleistocene Brawley and Ocotillo formations: evidence for initial strike-slip deformation along the San Felipe and San Jacinto Fault Zones, Southern California. Journal of Geology 115, 43–62.
Koepke, J., Berndt, J., Feig, S.T., Holtz, F., 2007. The formation of SiO_2-rich melts within the deep oceanic crust by hydrous partial melting of gabbros. Contributions to Mineralogy and Petrology 153 (1), 67–84.
Lachenbruch, A.H., Sass, J.H., Galanis Jr., S.P., 1985. Heat flow in southernmost California and the origin of the Salton Trough. JGR. Journal of Geophysical Research B 90 (8), 6709–6736.
Larsen, S., Reilinger, R., 1991. Age constraints for the present fault configuration in the Imperial-Valley, California—evidence for northwestward propagation of the Gulf of California rift System. Journal of Geophysical Research-Solid Earth and Planets 96 (B6), 10339–10346.
Li, H.C., Xu, X.M., Ku, T.L., You, C.F., Buchheim, H.P., Peters, R., 2008. Isotopic and geochemical evidence of palaeoclimate changes in Salton Basin, California, during the past 20 kyr: 1. (^{18}O and (^{13}C records in lake tufa deposits. Palaeogeography, Palaeoclimatology, Palaeoecology 259 (2–3), 182–197.
Lizarralde, D., Axen, G.J., Brown, H.E., Fletcher, J.M., González-Fernández, A., Harding, A.J., Holbrook, W.S., Kent, G.M., Páramo, P., Sutherland, F., Umhoefer, P.J., 2007. Variation in styles of rifting in the Gulf of California. Nature 448, 466–469.
Lonsdale, P.F., 1989. Geology and tectonic history of the Gulf of California. In: Winterer, E.L., Hussong, D.M., Decker, R.W. (Eds.), The Eastern Pacific Ocean and Hawaii. Geological Society of America, Boulder, pp. 499–521.
Lowenstern, J.B., Clynne, M.A., Bullen, T.D., 1997. Comagmatic A-type granophyre and rhyolite from the Alid Volcanic Center, Eritrea, Northeast Africa. Journal of Petrology 38, 1707–1721.
Lutz, A.T., Dorsey, R.J., Housen, B.A., Janecke, S.U., 2006. Stratigraphic record of Pleistocene faulting and basin evolution in the Borrego Badlands, San Jacinto fault zone, southern California. Geological Society of America Bulletin 118, 1377–1397.
McDowell, S.D., 1987. Geothermal alteration of sediments in the Salton Sea scientific drill hole—petrophysical properties and mass changes during alteration. Michigan Technological University Houghton, Michigan, Final Research Report for Department of Energy Grant DE-FG02-85ER13409, pp. 1–62.
McKibben, M.A., Hardie, L.A., 1997. Ore-forming brines in active continental rifts, In: Barnes, H.L. (Ed.), Geochemistry of Hydrothermal Ore Deposits, 3rd edition. Wiley, New York, pp. 877–935.
McKibben, M.A., Williams, A.E., Okubo, S., 1988. Metamorphosed Plio-Pleistocene evaporites and the origins of hypersaline brines in the Salton-Sea geothermal system, California—fluid inclusion evidence. Geochimica et Cosmochimica Acta 52 (5), 1047–1056.
Miller, J.S., Wooden, J.L., 2004. Residence, resorption and recycling of zircons in Devils Kitchen rhyolite, Coso volcanic field, California. Journal of Petrology 45 (11), 2155–2170.
Oskin, M., Stock, J., 2003. Pacific-north America plate motion and opening of the Upper Delfin Basin, northern Gulf of California, Mexico. Geological Society of America Bulletin 115 (10), 1173–1190.
Parsons, T., McCarthy, J., 1996. Crustal and upper mantle velocity structure of the Salton Trough, Southeast California. Tectonics 15 (2), 456–471.
Paces, J.B., Miller, J.D., 1993. Precise U–Pb ages of Duluth Complex and related mafic intrusions, northeastern Minnesota; geochronological insights to physical, petrogenetic, paleomagnetic, and tectonomagnetic processes associated with the 1.1 Ga Midcontinent Rift System. Journal of Geophysical Research 98, 13997–14013.
Reid, M.R., Coath, C.D., 2000. In situ U–Pb ages of zircons from the Bishop Tuff: no evidence for long crystal residence times. Geology 28 (5), 443–446.
Reid, M.R., Coath, C.D., Harrison, T.M., McKeegan, K.D., 1997. Prolonged residence times for the youngest rhyolites associated with Long Valley Caldera; ^{230}Th–^{238}U ion microprobe dating of young zircons. Earth Planetary Science Letters 150, 27–39.

Robinson, P.T., Elders, W.A., Muffler, L.J.P., 1976. Quaternary volcanism in the Salton Sea geothermal field, Imperial Valley, California. Geological Society of America Bulletin 87 (3), 347–360.

Sanudo-Wilhelmy, S.A., Flegal, A.R., 1994. Temporal variations in lead concentrations and isotopic composition in the Southern California Bight. Geochimica et Cosmochimica Acta 58 (15), 3315–3320.

Sarna-Wojcicki, A.M., Pringle, M.S., Wijbrans, J., 2000. New ^{40}Ar/^{39}Ar age of the Bishop Tuff from multiple sites and sediment rate calibration for the Matuyama–Brunhes boundary. Journal of Geophysical Research 105 (B9), 21,431–21,443.

Schmitt, A.K., 2007. Ion microprobe analysis of (^{231}Pa)/(^{235}U) and an appraisal of protactinium partitioning in igneous zircon. American Mineralogist 92 (4), 691–694.

Schmitt, A.K., Vazquez, J.A., 2006. Alteration and remelting of nascent oceanic crust during continental rupture: evidence from zircon geochemistry of rhyolites and xenoliths from the Salton Trough, California. Earth and Planetary Science Letters 252 (3–4), 260–274.

Schmitt, A.K., Grove, M., Harrison, T.M., Lovera, O.M., Hulen, J., Waters, M., 2003. The Geysers–Cobb Mountain magma system, California (Part 1): U–Pb zircon ages of volcanic rocks, conditions of zircon crystallization and magma residence times. Geochimica et Cosmochimica Acta 67 (18), 3423–3442.

Severson, L.K., 1987. Interpretation of Shallow Crustal Structure of the Imperial Valley, California, from Seismic Reflection Profiles. MSc Thesis University of California Berkeley: 1–68.

Simon, J.I., Reid, M.R., 2005. The pace of rhyolite differentiation and storage in an "archetypical" silicic magma system, Long Valley, California. Earth and Planetary Science Letters 235 (1–2), 123–140.

Smith, B., Sandwell, D., 2003. Coulomb stress accumulation along the San Andreas Fault system. Journal of Geophysical Research 108 (no.B6), 17.

Spulber, S.D, Rutherford, M.J., 1983. The origin of rhyolite and plagiogranite in oceanic crust; an experimental study. Journal of Petrology 24 (1), 1–25.

Sykes, G., 1937. The Colorado Delta. American Geographic Society, New York, p. 139.

Trail, D., Mojzsis, S.J., Harrison, T.M., Schmitt, A.K., Watson, E.B., Young, E.D., 2007. Constraints on Hadean zircon protoliths from oxygen isotopes, REEs and Ti-thermometry. Geochemistry Geophysics Geosystems (G-cubed) 8. doi:10.1029/2006GC001449.

Valley, J.W., 2003. Oxygen isotopes in zircon. Reviews in Mineralogy and Geochemistry 53, 343–385.

Zukin, J.G., Hammond, D.E., Ku, T.L., Elders, W.A., 1987. Uranium–thorium series radionuclides in brines and reservoir rocks from two deep geothermal boreholes in the Salton Sea geothermal field, southeastern California. Geochimica et Cosmochimica Acta 51 (10), 2719–2731.